Nano Energy 31 (2017) 90–95

Contents lists available at ScienceDirect

Nano Energy

journal homepage: www.elsevier.com/locate/nanoen

Iron diselenide nanoplatelets: Stable and efficient water-electrolysis catalysts

Rui Gao[a], Hao Zhang[a], Dongpeng Yan[a,b,*]

[a] State Key Laboratory of Chemical Resource Engineering, Beijing University of Chemical Technology, Beijing 100029, China
[b] Beijing Key Laboratory of Energy Conversion and Storage Materials, College of Chemistry, Beijing Normal University, Beijing 100875, China

ARTICLE INFO

Keywords:
Oxygen evolution reaction
Nanoplatelets
Iron diselenide
Density functional theory calculation

ABSTRACT

The development of efficient water-electrolysis catalysts plays a key role in clean and sustainable energy sources. In this work, 2D $FeSe_2$ nanoplatelets have been successfully synthesized via a hydrothermal reduction route, which exhibit extraordinarily high catalytic activities and stability for oxygen evolution reaction (OER). The remarkable electrocatalytic performance of $FeSe_2$ nanoplatelets (e.g., overpotential: 2.2 times higher than that of commercial RuO_2 at 500 mV; Tafel slope: 48.1 mV/dec; steady-state current densities remain constant after 70 h) can be attributed to highly exposed active sites associated with (210) crystal faces; the 2D nanostructure could also facilitate improvement of kinetics of water oxidation. Furthermore, the changes of energy level, band structure and water adsorption ability of $FeSe_2$ under different bias were further understood based on density functional theory calculation. Therefore, this work provides the first example of $FeSe_2$ nanoplatelets as OER application, which may open a new avenue to design and explore other Fe-based nanostructures as efficient catalysts for renewable energy.

1. Introduction

Hydrogen (H_2) is regarded as one of the most potential clean energy in the 21st century [1–3]. However, currently, more than 90% of hydrogen energy is obtained from fossil fuels [4–6]. As is known to all the burning of fossil fuels will highly increase the pollution of the environment and the crisis of global warming [7]. From a clean and sustainable perspective, water splitting is a low-cost and environmentally-friendly way to obtain hydrogen energy [8]. Generally, water electrolysis consists of two half reactions: 1) water oxidation and 2) proton reduction. The first half reaction is usually considered as the critical bottleneck in developing efficient electrolysis of water due to the inherent sluggish oxygen evolution reaction (OER) kinetics [9–12]. Thus, it is highly desirable to develop efficient electrocatalysts for OER, which has already attracted worldwide attention in recent years. To date, IrO_2 and RuO_2 are commonly considered as the most effective catalysts for OER in industry [13,14]. However, the low natural abundance and high cost have restricted the use of noble metal oxides in large scale water splitting technologies. Therefore, the development of earth-abundant OER electrocatalysts has become the new trend. Moreover, it was well-recognized that the interface and micro/nanostructures of the electrocatalysts have great effect on OER performance. i.e., the exposure of high catalytically active sites plays an important role in OER process.

Recently, the use of 2D layered nanostructures as OER catalysts has been paid much attention. For example, Sun et al. showed that the 2D g-C_3N_4 nanosheets with same catalyst loading give a higher current density (10.5 mA/cm^2) than bulk g-C_3N_4 [15], since the 2D nanosheets have higher specific surface area than bulk g-C_3N_4, thereby exposing more active sites for catalytic reaction. Song and Hu confirmed that the exfoliated 2D nickel iron and nickel cobalt layered double hydroxides nanosheets exhibit obvious higher activity and stability than the commercial iridium dioxide catalyst in oxygen evolution [16]. Xie et al. have developed 2D $CoSe_2$ nanosheets, which give a lower Tafel slope of 64 mV/dec, since the Co^{2+} ions are exposed on the surface and serve as the catalytically active sites [17]. Therefore, several 2D layered nanostructures present advantages of high-efficiency OER catalytic activity, due to the fully utilization of catalytic species and effective electron transfer at the interface/surface of electrocatalysts during water-splitting process.

From an elemental composition perspective, iron (Fe) has become one of the most promising non-noble metals for the design of robust OER catalysts [18,19], especially Fe-based 2D materials (such as metal hydroxide [20–22] and mixed-metal oxides [23]). Besides abundance and low cost, the excellent performance of Fe-based compounds derives from the intrinsic semiconductor/metal characters and unique

* Corresponding author at: State Key Laboratory of Chemical Resource Engineering, Beijing University of Chemical Technology, Beijing 100029, China.
E-mail addresses: yandp@bnu.edu.cn, yandp@mail.buct.edu.cn (D. Yan).

http://dx.doi.org/10.1016/j.nanoen.2016.11.021
Received 14 August 2016; Received in revised form 5 November 2016; Accepted 9 November 2016
Available online 13 November 2016

electronic structures, which could improve the electrical conductivity and the adsorption of H_2O. For example, Driess et al. [23] reported the 2D cobalt iron oxides material could achieve obviously higher catalytic performance in the kinetics regime, in terms of onset potential and diffusing limiting current density. Dai et al. have reported a 2D nickel–iron layered double hydroxide (NiFe-LDH)–carbon nanotube (CNT) complex with higher OER catalytic activity and stability than commercial Ir-based catalysts [20]. The high catalytic activity can be attributed to the formation of ultrathin 2D nanoplates of a highly OER-active NiFe-LDH structure. Therefore, the design of idealized 2D Fe-based catalysts with high exposure of active sites could be a facile strategy to develop high-efficiency water electrolysis.

In the meantime, very recently, several bulk metal selenides (such as NiSe and $CoSe_2$ materials) with good OER catalytic performance are reported [24–26]. To combine the advatanges of Fe-based 2D materials and metal selenides, herein, iron diselenide ($FeSe_2$) nanocrystals have been selected as the model system, which can be synthesized via a hydrothermal reduction route. The as-prepared $FeSe_2$ nanocrystals present highly tunable micro/nano-sized morphologies, which were further transferred onto a nickel substrate as OER catalysts. $FeSe_2$ nanoplatelet-based electrocatalyst shows a much lower overpotential (of 330 mV to achieve 10 mA/cm^2). At 500 mV overpotential, the current density of $FeSe_2$ nanoplatelets is 70 mA/cm^2, which is 2.2 times higher than that of commercial RuO_2, strongly demonstrating the high electrocatalytic activity of 2D $FeSe_2$ nanoplatelets. Furthermore, the steady-state current densities of the $FeSe_2$ still remain constant even after 70 h at high potential (1.67 V), and the linear sweep voltammetry (LSV) curve of $FeSe_2$ nanoplatelets almost has no decrease. In addition, the changes of energy levels and electronic structures of $FeSe_2$ under different bias were further analyzed based on the theoretical studies. To the best of our knowledge, this is the first example of $FeSe_2$ nanoplatelets towards high-efficiency OER application.

2. Experimental section

2.1. Synthesis of $FeSe_2$ and $CuSe_2$

The synthesis of MSe_2 (M=Fe and Cu) was based on a mild solution approach: Mixing aqueous solutions consisting of Se powder and metal chlorides were made according to stoichiometric ratios ($FeSe_2$: 0.03 g of Se and 0.06 g of $FeCl_3{\cdot}6H_2O$; $CuSe_2$: 0.0240 g of Se powders and 0.08 g of $CuCl_2{\cdot}6H_2O$). The total volume of reagent solution was adjusted to 70 mL by adding deionized water. 5 mL of hydrazine hydrate (98 wt%) was then dropped into the above solution. After vigorous agitating for 10 min, the reactant was transferred into a 100 mL of Teflon–lined autoclave, which was sealed and maintained at different temperatures (120 °C; 150 °C; 180 °C; 210 °C for $FeSe_2$, and 180 °C for $CuSe_2$) for 24 h and then naturally cooled to room temperature. The final product was collected and washed with distilled water and absolute ethanol for many times, and dried in vacuum at 60 °C overnight for further characterization.

2.2. Characterization

Powder X-ray diffraction (XRD) patterns of all the samples were carried out using a graphite-filtered Cu Kα radiation operating at 40 kV and 30 mA, λ=0.15418 nm (Rigaku X-ray diffractometer). X-ray photoelectron spectrometry (XPS) was recorded using Al Kα radiation (Thermo VG ESCALAB MK II). The positions of all binding energies were calibrated by using the C 1 s line at 284.8 eV. Scanning electron microscopy with an accelerating voltage of 20 kV (SEM, ZeissSUPRA 55) was applied for detailed morphology analyses. TEM and EDS mappings were taken using microscopy (JEOL JEM-2010F) combined with an EDX (Oxford X-MaxN 80-TLE) spectroscopy.

2.3. Preparation of RuO_2 electrodes

A homogeneous catalyst was obtained by sonication of 2 mg RuO_2, 0.5 mL water, 30 μL 5 wt% Nafion solution, and 0.5 mL ethanol for 30 min. Then, 5 μL of the dispersion (containing 10 μg of catalyst) was loaded on the surface of a nickel piece (surface area: 1 cm^2). Consequently, the overall RuO_2 electrode loads amount of 10 μg cm^{-2}.

2.4. Electrochemical measurements

All electrochemical measurements were carried out on the electrochemical workstation (CHI 660 C, CH Instrument Co. USA). Ag/AgCl and Pt wire were used as the reference and counter electrodes, respectively. Typically, 2 mg of catalyst and 30 μL Nafion solution (Sigma Aldrich, 5 wt%) were dispersed into 1 mL water-ethanol solution with volume ratio of 1:1 by sonicating for at least 0.5 h to form a homogeneous ink. Then, 5 μL of the dispersion (containing 10 μg of catalyst) was loaded onto a 1×1 cm^2 pure nickel piece (the pure nickel piece was cleaned by sonication with acetone for 30 min firstly, then sonicated by hydrochloric acid (30wt%) for 2 min. Linear sweep voltammetry with a scan rate of 10 mV/s was conducted in 1 M KOH. The KOH electrolyte was degassed by bubbling oxygen for 30 min. All of the potentials were calibrated to a reversible hydrogen electrode (RHE). Cyclic voltammetry (CV) was performed at various scan rates (4, 40, 80, 120, 160 and 200 mV/s, etc) in 0.61–0.74 V vs. RHE region. The double-layer capacitance (C_{dl}) was estimated by plotting the Δj (j_a-j_c) at 0.67 V vs. RHE against the scan rates, in which the j_a and j_c are the anodic and cathodic current density, respectively. The slope is twice that of the double-layer capacitance C_{dl}. For water splitting, $FeSe_2$ and $CuSe_2$ electrocatalyst were used as working electrode in a three-electrode system. The Faradaic efficiency was calculated by comparing the amount of gas theoretically calculated and experimentally measured. To assess the Faradic efficiency, we collected O_2 by water-gas displacing method, and calculated the mole values of O_2 generated from the water splitting. And then we calculated the theoretical amount of O_2 with I–t curve by applying the Faraday law.

2.5. Calculated details

Periodic density functional theory (PDFT) calculations of the electronic properties for idealized $FeSe_2$ model (Scheme S1a) under different bias potentials (0–0.182 V/nm: corresponding to 0–2 V in experiment conditions considering the thickness of 11 nm for the $FeSe_2$ nanoplatelets) were performed using Dmol3 [27,28] module in Material Studio software package.[29] The geometric configuration was optimized by Perdew-Wang (PW91) [30] generalized gradient approximation (GGA) method with the double numerical basis sets plus polarization function (DNP). The core electrons for metals were treated by effective core potentials (ECP). SCF converged criterion was within 1.0×10^{-5} hartree/atom and the converged criterion of structure optimization was 1×10^{-3} hartree/bohr. The Brillouin zone is sampled by 1×1×1 k-points, and test calculations reveal that the increase of k-points does not influence the results. For calculations of adsorption energy of water, the (210) crystal face of $FeSe_2$ (Scheme S1b, with three atomic layers) were modeled with vacuum widths of 15 Å.

3. Results and discussion

The hydrothermal synthesis process of $FeSe_2$ was performed at different temperatures, in which hydrated iron chloride was employed to supply Fe source, and aqueous hydrazine ($N_2H_4{\cdot}H_2O$) was used as reducing agent (Fig. 1). As shown in Fig. 2a and Fig. S1, all the X-ray diffraction (XRD) peaks of the obtained powder samples are consistent with the $FeSe_2$ phase (JCPDS Card No. 21-0432), which can be indexed as orthorhombic crystal system (*Pnnm* space group and *mmm* point

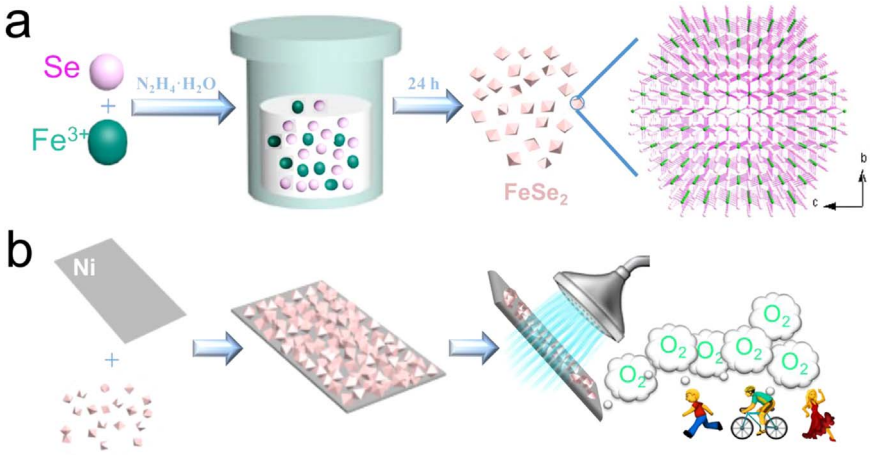

Fig. 1. Schematic illustration of the formation of $FeSe_2$ nanoplatelets (a) and its application in OER (b).

group), suggesting the high purity of the resulting samples.

The morphology of the as-prepared $FeSe_2$ at different hydrothermal conditions was further investigated with scanning electron microscopy (SEM, Fig. S2 and Fig. 2b), which shows different shapes and sizes. There is a trend that the $FeSe_2$ nanocrystals exhibited 1D rods (120 °C) across 2D platelets (150 and 180 °C) and then to the bulk and/or aggregation states (210 °C) upon the increasing temperatures. Typically, the $FeSe_2$ (180 °C) is more likely rhombic nanoplatelet structures among the obtained $FeSe_2$ samples, which was naturally speculated that the nanoplatelets may expose more catalyst active sites relative to the bulk form. Moreover, the elemental composition of the materials can be confirmed by the energy dispersive spectrum (EDS), which clearly shows Fe and Se components (Fig. S3). For the $FeSe_2$ (180 °C) with the lowest overpotential value as shown below, transmission electron microscopy (TEM) reveals that the particle size is around 450 nm (Fig. 2c). Moreover, high-resolution TEM (HRTEM) reveals lattice fringes with a spacing of 0.223 nm, indexed as (210) planes of $FeSe_2$ (Fig. 2d). Atomic force microscopy (AFM) and the corresponding height profile (Fig. 2e) show that the average thickness is around 11 nm, further confirming the 2D nanoplatelet morphology of the $FeSe_2$. Scanning TEM-energy dispersive X-ray spectroscopy (STEM-EDX) elemental mapping indicated a relatively homogenous distribution of Fe and Se elements within the single rhombic nanoplatelet (Fig. 2f).

The X-ray photoelectron spectroscopy (XPS) measurement was carried out to obtain the information on electronic structures and chemical states. Fig. S4b shows the Se 3d spectrum of $FeSe_2$, in which the binding energy at 54.3 eV is attributed to the Fe–Se bond. The peaks at 55.8 and 59.2 eV correspond to Se $3d_{5/2}$ (Se–Se) and Se $3d_{3/2}$, respectively. Fig. S4a shows the the Fe $2p_{3/2}$ signal, which can be fitted as two chemical states with binding energies of 706.5 and 711.4 eV. The dominant peak at 706.5 eV in the Fe $2p_{3/2}$ XPS indicates the presence of Fe–Fe interactions, and the relatively weak peak at 711.4 eV is derived from Fe^{3+} coordinated Se ions. The peaks at 719.8 and 724.6 eV are assigned to Fe $2p_{1/2}$.

The next goal is to study the electrochemical water oxidation performances of as-obtained $FeSe_2$ nanocrystals. To effectively illustrate the role of Fe element on the electrocatalytic performance, we also synthesized $CuSe_2$ at 180 °C which has the same crystal structure with $FeSe_2$ (Fig. S5). SEM and TEM also reveal that the particle size of 2D $CuSe_2$-180 °C nanoplatelets is about 450 nm, which is similar to the $FeSe_2$-180 °C (Figs. S6 and S7). HRTEM image (Fig. S6) and XRD patterns (Fig. S8) evidence the pure $CuSe_2$ phase (JCPDS Card No. 19-0400). In addition, the element composition of the materials can be confirmed by the EDS (Fig. S9). The SEM elemental mapping indicates a relatively homogenous distribution of each element along the $CuSe_2$ surface (Fig. S10). Moreover, commercial RuO_2 was chosen as the standard sample to compare with $FeSe_2$. As shown in Fig. S11a, XRD peaks of the powder sample are consistent with the RuO_2 phase (JCPDS Card No. 40-1290), which can be indexed as orthorhombic crystal system (*mnm* point group), suggesting the high purity of the resulting samples. TEM reveals that the particle size is around 150 nm (Fig. S11b). Moreover, HRTEM shows lattice fringes with a spacing of 0.253 nm, indexed as (110) plane of RuO_2 (Fig. S11c).

The electrocatalytic OER was examined in 1.0 M KOH solution using a typical three-electrode system (Supporting Information for experimental details). As revealed in Fig. 3a, $FeSe_2$ nanoplatelet-based electrocatalyst shows a much lower overpotential (of 330 mV to achieve 10 mA/cm^2). In contrast, pure Ni, $CuSe_2$ nanoplatelet, and commercial RuO_2 (require 610, 580, and 510mA/cm, respectively. It is also noted that the FeSe prepared at different temperatures (120, 150, 180, and 210°C) all present relative low overpotential at large current densities (above 10 mA/cm^2) compared with commercial RuO_2 (Fig. S12 and Fig. 3a). At 500 mV overpotential, the current density of $FeSe_2$ nanoplatelets is 70 mA/cm^2, which is 2.2 and 8.7 times higher than the commercial RuO_2 and $CuSe_2$ nanoplatelet, respectively. These observations strongly demonstrate the high electrocatalytic activity of 2D $FeSe_2$ nanoplatelets, which shows the lowest overpotential among different morphologies of the $FeSe_2$. Moreover, the Tafel slope (48.1 mV/dec) of $FeSe_2$ nanoplatelets is lowest among other $FeSe_2$ samples (87.2, 64.5, and 55.0 mV/dec) obtained at other temperatures (Fig. S13 and Fig. 3c). In addition, the Tafel slopes of $FeSe_2$ nanoplatelets is also much lower than the RuO_2 (84.5 mV/dec) and $CuSe_2$ (214.8 mV/dec) counterparts. The lower Tafel slope further confirms that $FeSe_2$ nanoplatelets present faster kinetics of water oxidation.

The steady-state current densities of the $FeSe_2$ remain constant even after 70 h (Fig. 3b and Fig. S14), in which the linear sweep voltammetry (LSV) curve of $FeSe_2$ almost appeared overlapping with the initial state (inset of Fig. 3b and Fig. S14). In contrast, the steady-state current densities of the $CuSe_2$ nanoplatelets only maintained 45 h at the same voltage with $FeSe_2$ (Fig. S15). The XRD patterns (Fig. S16) show that the typical diffraction peaks of the material are still associated with $FeSe_2$ after 70 h. STEM-EDX spectra illustrate that the morphology of the sample nearly remains the same before and after OER, but the Se content decreases slightly from 68.69% to 58.20% (Fig. S17 and Fig. S18) after OER cycling. Although the bulk structure and morphology maintains, the slight loss of Se content may suggest the partial oxidation of surface $FeSe_2$ into metal oxide under high oxidizing potential. Recently, Hu et al. reported that NiSe has a trend to transfer into NiO under electrochemical process;[31] the OER activity and stability of $FeSe_2$ in this work may be different from the NiSe system. Additionally, after long-term cycling, it was observed that the emergence of a redox peak (≈1.43 V) in the pre-OER region, particularly for

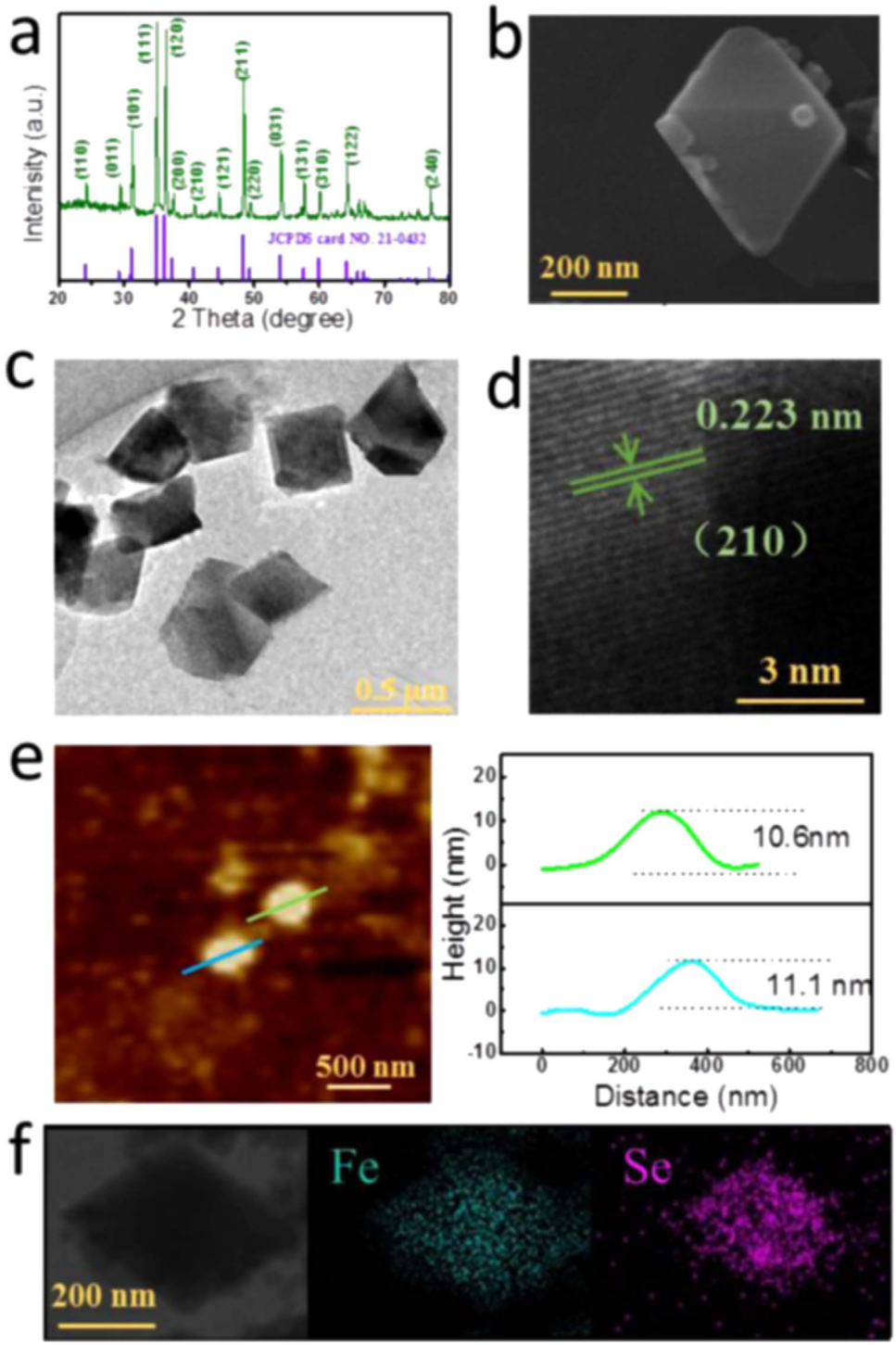

Fig. 2. (a) XRD pattern, (b) SEM image, (c) TEM image, (d) HRTEM image, (e) AFM image and the corresponding height profiles, (f) STEM-EDX elemental mapping of $FeSe_2$-180 °C nanoplatelets.

$FeSe_2$-210 °C system (inset Fig. S14). This can be assigned to the Ni(II)/Ni(III or IV) redox process [19], since the anchoring force between the aggregate state of $FeSe_2$ and substrate was relatively weak, and thus a bit of Ni species may be exposed and actived during OER. Furthermore, $FeSe_2$ nanoplatelets show nearly 100% Faradaic efficiency for OER (Fig. 3d) at high overpotentia (500 mV). In addition, double layer capacitance (C_{dl}) measurements were conducted to estimate the electrochemical active areas. $FeSe_2$ nanoplatelets show a C_{dl} of 1.09 mF/cm, much higher than that of $CuSe_2$ sample (0.48 mF/cm^2, Fig. S19), revealing that the $FeSe_2$ nanoplatelets has an advantage in enlarging the active surface area associated with more catalytic active sites than $CuSe_2$. These results provide effective evidences for long-term stability and hence showing perspective potential for practical applications.

To better understand the electronic structure and water adsorption energy of $FeSe_2$ nanoplatelets at different external potentials, periodic density functional theoretical (PDFT) studies were performed on the idea model. Total and partial electronic densities of states (PDOS and TDOS, Fig. 4a and Fig. S20, S21) show that the $FeSe_2$ system has a small band gap of 2.3 eV. The top of the valence band (VB) is mainly

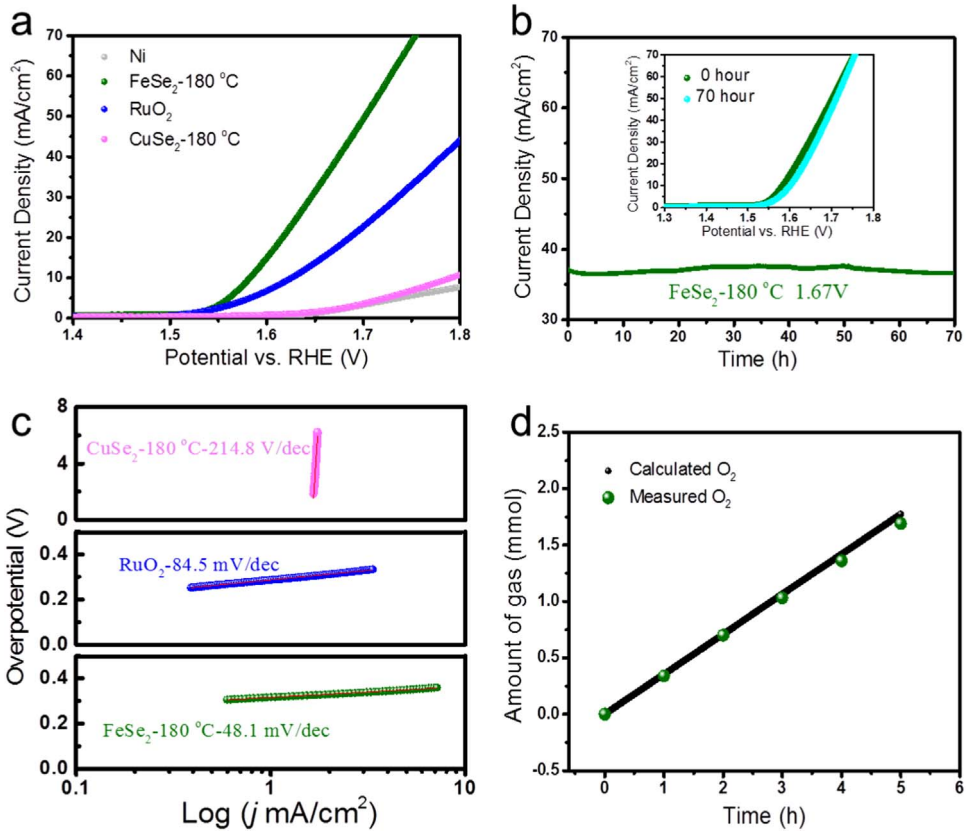

Fig. 3. Electrochemical properties for the $FeSe_2$-180 °C nanoplatelets. (a) Polarization curves. (b) *I–t* curve at 1.67 V versus reversible hydrogen electrode (RHE). Inset is polarization curves before and after 70 h *I–t* curve. (c) The corresponding Tafel plots. (d) The amount of gas (theoretically calculated and experimentally measured) versus time for water splitting.

dominated by the *d* atomic orbitals of Fe, while the bottom of the conducting band (CB) is mainly contributed from both the *d* orbitals in Fe and *p* orbitals in Se. This result suggests that the occurrence of *d*-*d* transition of Fe and electronic transfer between Fe and Se. Upon adding the external bias (ca 0–2 V, in the experimental range), PDOS and TDOS of Fe located at around −1 eV present an obvious shift towards negative direction (Fig. 4a), confirming the redistribution of the VB occurs, while the CB remains the same under external potential,

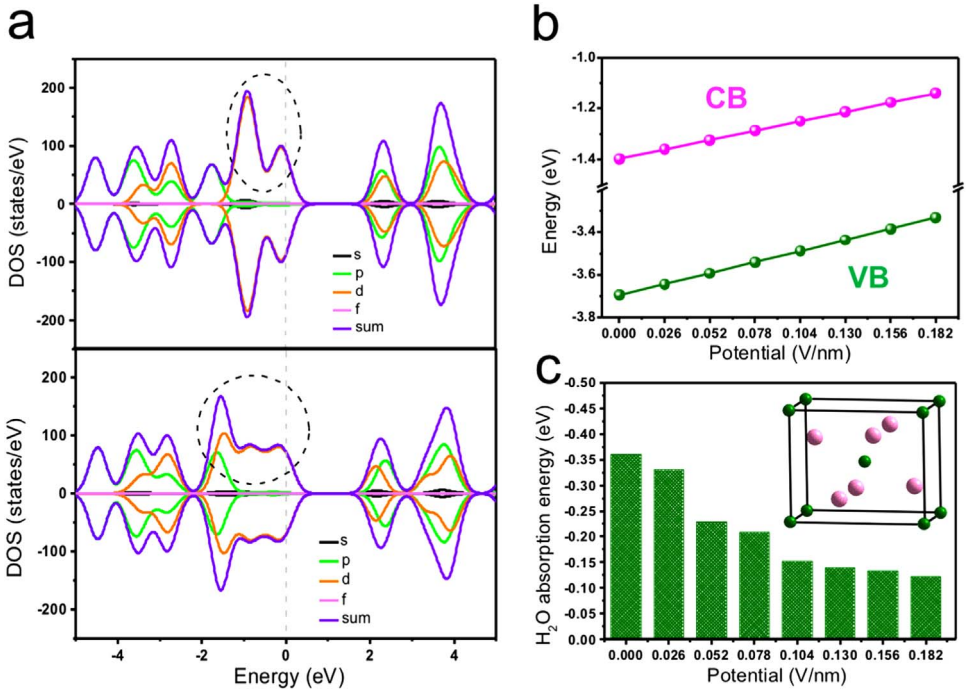

Fig. 4. (a) Total and partial electronic density of states (TDOS and PDOS) calculated for $FeSe_2$ under 0 V (top) and 2 V (down). (b) The VB (green color) –CB (pink color) energy of $FeSe_2$ under different bias. (c) Calculated adsorption energies of H_2O on the (210) surface of $FeSe_2$ under different bias. (inset: atomic structure model of $FeSe_2$, with the Fe atoms at the corners and in the center, the Se atoms at the face centers).

suggesting that the electronic structure of Fe element in $FeSe_2$ is highly tunable. Moreover, both the CB and VB positions have an increasing trend upon increasing the bias potential (Fig. 4b), with the band gap values decrease slightly at a high potential (2 V, Fig. 4b and Fig. S22). Moreover, the adsorption energy of water molecules on the (210) crystal face (experimental condition) decreases slightly as the potential increases (Fig. 4c), indicating that the external electric potential does not present obvious influence on the effective water adsorption on electrocatalyst.

4. Conclusion

In summary, we report a facile synthesis of $FeSe_2$ nanoplatelets by hydrothermal reduction route. The $FeSe_2$ nanoplatelets exhibit highly enhanced OER catalytic activity compared with $CuSe_2$ nanoplatelets and commercial RuO_2. The excellent performance of $FeSe_2$ nanoplatelets derives from the intrinsic semiconductor properties and tunable electronic structures, which reduce the OER overpotential. Moreover, the nano-sized 2D platele-like morphology could also increase the availability of active sites for electrocatalysis. PDFT calculation also promotes the detailed insight into the energy level and water adsorption at the surface of $FeSe_2$ nanoplatelets. Therefore, experimental and theoretical studies prove that $FeSe_2$ is a very promising, noble metal-free electrocatalyst for water splitting and energy conversion.

Acknowledgements

This work was supported by the 973 Program (Grant No. 2014CB932103), the National Natural Science Foundation of China (NSFC) (Grant No. 21301016, 21473013), and the Beijing Municipal Natural Science Foundation (Grant No. 2152016).

Appendix A. Supporting information

Supplementary data associated with this article can be found in the online version at doi:10.1016/j.nanoen.2016.11.021.

References

[1] A.J. Bard, M.A. Fox, Acc. Chem. Res. 28 (1995) 141–145.
[2] M.G. Walter, E.L. Warren, J.R. McKone, S.W. Boettcher, Q. Mi, E.A. Santori, N.S. Lewis, Chem. Rev. 110 (2010) 6446–6473.
[3] M. Dresselhaus, I. Thomas, Nature 414 (2001) 332–337.
[4] W. Winsche, K.C. Hoffman, F. Salzano, Science 180 (1973) 1325–1332.
[5] J.A. Turner, Science 305 (2004) 972–974.
[6] D. Kim, K.K. Sakimoto, D. Hong, P. Yang, Angew. Chem. Int. Ed. 54 (2015) 3259–3266.
[7] B. Rausch, M.D. Symes, G. Chisholm, L. Cronin, Science 345 (2014) 1326–1330.
[8] N.S. Lewis, D.G. Nocera, Proc. Nat. Acad. Sci. 103 (2006) 15729–15735.
[9] F. Jiao, H. Frei, Angew. Chem. Int. Ed. 48 (2009) 1841–1876.
[10] A. Ramırez, P. Bogdanoff, D. Friedrich, S. Fiechter, Nano Energy 1 (2012) 282–289.
[11] Y. Zhu, W. Zhou, Y. Chen, J. Yu, M. Liu, Z. Shao, Adv. Mater. 27 (2015) 7150–7155.
[12] K. Qua, Y. Zheng, S. Dai, S.Z. Qiao, Nano Energy 19 (2016) 373–381.
[13] C.C.L. McCrory, S. Jung, J.C. Peters, T.F. Jaramillo, J. Am. Chem. Soc. 135 (2013) 16977–16987.
[14] J. Wang, H.X. Zhong, Y.L. Qin, X.B. Zhang, Angew. Chem. Int. Ed. 125 (2013) 5356–5361.
[15] J. Tian, Q. Liu, A.M. Asiri, K.A. Alamry, X. Sun, ChemSusChem 7 (2014) 2125–2130.
[16] F. Song, X. Hu, Nat. Commun. 5 (2014) (4477-4477).
[17] L. Liang, H. Cheng, F. Lei, J. Han, S. Gao, C. Wang, Y. Sun, S. Qamar, S. Wei, Y. Xie, Angew. Chem. Int. Ed. 54 (2015) 12004–12008.
[18] J.L. Fillol, Z. Codola, I. Garcia-Bosch, L. Gomez, J. Jose Pla, M. Costas, Nat. Chem. 3 (2011) 807–813.
[19] J. Suntivich, K.J. May, H.A. Gasteiger, J.B. Goodenough, Y. Shao-Horn, Science 334 (2011) 1383–1385.
[20] M. Gong, Y. Li, H. Wang, Y. Liang, J.Z. Wu, J. Zhou, J. Wang, T. Regier, F. Wei, H. Dai, J. Am. Chem. Soc. 135 (2013) 8452–8455.
[21] J.S. Luo, J.H. Im, M.T. Mayer, M. Schreier, M.K. Nazeeruddin, N.G. Park, S.D. Tilley, H.J. Fan, M. Grätzel, Science 345 (2014) 1593–1596.
[22] X. Jia, Y. Zhao, G. Chen, L. Shang, R. Shi, X. Kang, G.I.N. Waterhouse, L. Wu, C. Tung, T. Zhang, Adv. Energy Mater. 20 (2016) 1502585–1502591.
[23] A. Indra, P.W. Menezes, N.R. Sahraie, A. Bergmann, C. Das, M. Tallarida, D. Schmeisser, P. Strasser, M. Driess, J. Am. Chem. Soc. 136 (2014) 17530–17536.
[24] C. Tang, N. Cheng, Z. Pu, W. Xing, X. Sun, Angew. Chem. Int. Ed. 54 (2015) 9351–9355.
[25] A.T. Swesi, J. Masud, M. Nath, Energy Environ. Sci. 9 (2016) 1771–1782.
[26] I.H. Kwak, et al., ACS Appl. Mater. Interfaces 8 (2016) 5327–5334.
[27] B. Delley, J. Chem. Phys. 92 (1990) 508.
[28] B. Delley, J. Chem. Phys. 113 (2000) 7756–7764.
[29] Dmol3 Module, MS Modeling, Version 2.2; Accelrys Inc.: San, Diego, CA, 2003.
[30] J.P. Perdew, J.A. Chevary, S.H. Vosko, K.A. Jackson, M.R. Pederson, D.J. Singh, C. Fiolhais, Phys. Rev. B 46 (1992) 6671–6687.
[31] X. Xu, F. Song, X. Hu, Nat. Commun. 7 (2016) 12324–12330.

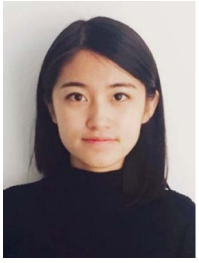

Rui Gao obtained her BS degree at Beijing University of Chemical Technology (BUCT, China) in 2013. She is currently a PhD student under the supervision of Prof. Acad. Xue Duan and Prof. Dongpeng Yan at the State Key Laboratory of Chemical Resource Engineering Beijing University of Chemical Technology (BUCT, China). Her research interests are the design and synthesis of nanostructured materials for photoemission and photo-electrochemistry.

Hao Zhang obtained his MS degree under the supervision of Prof. Dongpeng Yan at the State Key Laboratory of Chemical Resource Engineering, Beijing University of Chemical Technology (BUCT, China) in 2016. His research topics are polyurethane materials and nanostructured materials for electrochemistry.

Professor Dongpeng Yan obtained his Ph.D. degree under the supervision of Prof. Acad. Xue Duan at Beijing University of Chemical Technology (BUCT, China) in 2012. Then, he became an associate professor at BUCT. In 2014, he moved to Beijing Normal University (China) as a full professor. In 2011 and 2013, as a visiting scholar, he has studied at University of Cambridge (UK) and University College London (UK). His research topics are functional molecular materials, host-guest chemistry and photo-electrochemistry. He was received the Tang Aoqing Chemical Scholarship (2011), and an Outstanding Doctoral Dissertation Prize in Beijing (2013) amongst others